Journal of Geophysical Research: Oceans

RESEARCH ARTICLE
10.1029/2018JC014037

Special Section:
Forum for Arctic Modeling and Observational Synthesis (FAMOS) 2: Beaufort Gyre phenomenon

Partitioning of Kinetic Energy in the Arctic Ocean's Beaufort Gyre

Mengnan Zhao[1], **Mary-Louise Timmermans**[1], **Richard Krishfield**[2], **and Georgy Manucharyan**[3]

[1]Department of Geology and Geophysics, Yale University, New Haven, CT, USA, [2]Woods Hole Oceanographic Institution, Woods Hole, MA, USA, [3]Division of Geological and Planetary Sciences, California Institute of Technology, Pasadena, CA, USA

Key Points:
- Mooring measurements of velocity are analyzed to quantify kinetic energy in the Beaufort Gyre
- Water column kinetic energy is dominated by eddies with most energy found in the first two baroclinic modes
- It is shown how the partitioning of kinetic energy is related to the Beaufort Gyre halocline stratification

Correspondence to:
M. Zhao,
mengnan.zhao@yale.edu

Citation:
Zhao, M., Timmermans, M.-L., Krishfield, R., & Manucharyan, G. (2018). Partitioning of kinetic energy in the Arctic Ocean's Beaufort Gyre. *Journal of Geophysical Research: Oceans*, *123*, 4806–4819. https://doi.org/10.1029/2018JC014037

Received 2 APR 2018
Accepted 31 MAY 2018
Accepted article online 20 JUN 2018
Published online 10 JUL 2018

Abstract Kinetic energy (KE) in the Arctic Ocean's Beaufort Gyre is dominated by the mesoscale eddy field that plays a central role in the transport of freshwater, heat, and biogeochemical tracers. Understanding Beaufort Gyre KE variability sheds light on how this freshwater reservoir responds to wind forcing and sea ice and ocean changes. The evolution and fate of mesoscale eddies relate to energy pathways in the ocean (e.g., the exchange of energy between barotropic and baroclinic modes). Mooring measurements of horizontal velocities in the Beaufort Gyre are analyzed to partition KE into barotropic and baroclinic modes and explore their evolution. We find that a significant fraction of water column KE is in the barotropic and the first two baroclinic modes. We explain this energy partitioning by quantifying the energy transfer coefficients between the vertical modes using the quasi-geostrophic potential vorticity conservation equations with a specific background stratification observed in the Beaufort Gyre. We find that the quasi-geostrophic vertical mode interactions uphold the persistence of KE in the first two baroclinic modes, consistent with observations. Our results explain the specific role of halocline structure on KE evolution in the gyre and suggest depressed transfer to the barotropic mode. This limits the capacity for frictional dissipation at the sea floor and suggests that energy dissipation via sea ice-ocean drag may be prominent.

1. Introduction

The Canada Basin's Beaufort Gyre has accumulated a significant amount of freshwater over the past two decades under the prevailing anticyclonic wind forcing and Ekman transport convergence (e.g., Krishfield et al., 2014; Proshutinsky et al., 2009). The freshwater content is associated with a strong halocline stratification in the region, isolating the surface ocean layer and sea ice from deep ocean heat fluxes, and its storage and release also have climate implications beyond the Arctic Ocean (e.g., Proshutinsky et al., 2015). As anticyclonic wind forcing spins up the gyre, a significant fraction of energy is stored in the form of available potential energy, manifest by the steepening of isopycnals. This available potential energy can be released via baroclinic instability and the generation of eddies (i.e., kinetic energy, KE; e.g., Holland, 1978; Manucharyan & Spall, 2015; Pedlosky, 1979).

Mesoscale eddies are ubiquitous in the Beaufort Gyre, residing within the stratified halocline (e.g., Pickart et al., 2005; Timmermans et al., 2008; Zhao & Timmermans, 2015; Zhao et al., 2014). These eddies have diameters around 10 km of the same order of magnitude as the first and second baroclinic Rossby deformation radii (see Zhao et al., 2014). The eddies have azimuthal speeds typically exceeding 15 cm/s and are observed far from their presumed origins at the gyre boundaries and are assumed to be translated to the basin interior (e.g., Manley & Hunkins, 1985; Manucharyan & Timmermans, 2013; Timmermans et al., 2008; Zhao et al., 2014). It remains unclear how the KE of mesoscale eddies is ultimately dissipated. One could argue, for example, that eddies dissipate by friction at the bottom or top (e.g., the underside of sea ice) ocean boundaries. However, they are observed to reside within the stratified halocline and would therefore have to first become surface intensified or barotropize.

Geostrophic turbulence theory suggests that in a uniform stratification, KE can be redistributed in the water column giving rise to flows that are uniform in depth (e.g., Charney, 1971; Vallis, 2006); this allows for the dissipation of energy by bottom drag. The redistribution involves vertical exchange of KE over the water column. Because the vertical structure of the horizontal velocity can be decomposed into an orthogonal basis, which

depends on the ambient stratification, the partitioning of KE into vertical normal modes (i.e., barotropic and baroclinic modes) is often employed to study this process (e.g., Flierl, 1978; Hua & Haidvogel, 1986). Here we invoke the same formalism to explore the distribution and evolution of KE in the Beaufort Gyre halocline.

In a study of observations confined to the midlatitudes (between ~20°N and ~50°N), Wunsch (1997) partitions KE measured from moorings into vertical dynamic water column modes (estimated from the mean stratification) and finds that most of the water column KE is contained in the barotropic and first baroclinic modes. This may be explained by geostrophic turbulence in a nonuniformly stratified water column. Smith and Vallis (2001), for example, find that surface-intensified stratification associated with the thermocline impedes the efficiency of KE transfer to the barotropic mode and results in a concentration of energy in the first baroclinic mode. The ubiquitous intrahalocline eddy field in the Beaufort Gyre indicates a distinct energy pathway from the cases examined by Smith and Vallis (2001) and Wunsch (1997), for example, which are dominated by surface eddies. In this paper, we analyze mooring measurements spanning 2003–2016 to investigate how the Beaufort Gyre KE distribution relates to its stratification. Specifically, because the average water column KE is dominated by the existence of halocline eddies (e.g., Zhao et al., 2014, 2016), we seek to examine how the KE of the eddies is redistributed among different modes and how this may relate to gyre energetics.

The paper is outlined as follows. The Beaufort Gyre mooring measurements and auxiliary data are described in section 2. In section 3, vertical water column barotropic and baroclinic modes are introduced and calculated from the mean stratification. It is further instructive to contrast these results with modes calculated for a typical stratification in the North Pacific Ocean, which we take as a representative of the midlatitudes. KE inferred from mooring velocity measurements is separated into these vertical modes in section 4. Next, we seek to interpret results of the KE partitioning. To this end, in section 5, conservation of quasi-geostrophic potential vorticity is considered and interaction coefficients (which provide information on the efficiency of energy transfer between different vertical modes and depend upon stratification) are compared between the Beaufort Gyre and the North Pacific. In section 6, we summarize and discuss the limitations and implications of our findings.

2. Measurements

2.1. Moored Measurements

The primary data used in this study are moored measurements from the Beaufort Gyre Exploration Project (BGEP, http://www.whoi.edu/beaufortgyre) between August 2003 and 2016. A total of four moorings (denoted A, B, C, and D) is deployed across the Beaufort Gyre (Figure 1a). A McLane Moored Profiler (MMP) on each mooring returns profiles of pressure, temperature, salinity, and velocity from around 50-90m to ~2,000m depth. The data are processed to a vertical resolution of ~2 m, and profiles are returned every ~6 h and then ~48 h (see Proshutinsky et al., 2009, for further details). The background geostrophic flow in the Beaufort Gyre is relatively weak (compared to typical velocities associated with mesoscale eddies as will be shown), on the order of a few cm/s, perhaps somewhat larger in recent years as a result of the intensification of the gyre flow (e.g., Armitage et al., 2017; Zhang et al., 2016), and the magnitude of the flow decreases with depth. Moorings closer to topographic boundaries (Moorings B and D) record higher velocities in general (Figure 1a). Velocity data are nominally accurate to ±2 cm/s, but our primary interest here is understanding the distribution of KE (i.e., relative, rather than absolute values) and the accuracy does not affect our results.

2.2. Auxiliary Data

In addition to mooring measurements, hydrographic CTD data from the annual BGEP/Joint Ocean Ice Studies expedition (http://www.whoi.edu/beaufortgyre) are used to extrapolate density profiles from the mooring measurements (i.e., shallower than ~50 m and deeper than ~2,000 m to the full water column depth), as required for the calculation of vertical mode structures (see Appendix A). Pressure, temperature, and salinity are measured each summer/fall at sites throughout the Beaufort Gyre (including at mooring locations). Data from Ice-Tethered Profilers (ITPs; see Krishfield et al., 2008; Toole et al., 2011), drifting year-round in the Beaufort Gyre making measurements of temperature and salinity between ~7 and ~750 m, are used to examine the influence of the seasonality of the surface stratification on the structure of the vertical modes.

Because the moorings do not provide surface velocity data, we use velocity information from the reanalysis product TOPAZ4 of the Copernicus Marine Environment Monitoring Service (marine.copernicus.eu) to supplement mooring velocities. The product is generated via the HYCOM model coupled to a sea ice model, assimilated with in situ measurements and satellite data from various systems (see Sakov et al., 2017).

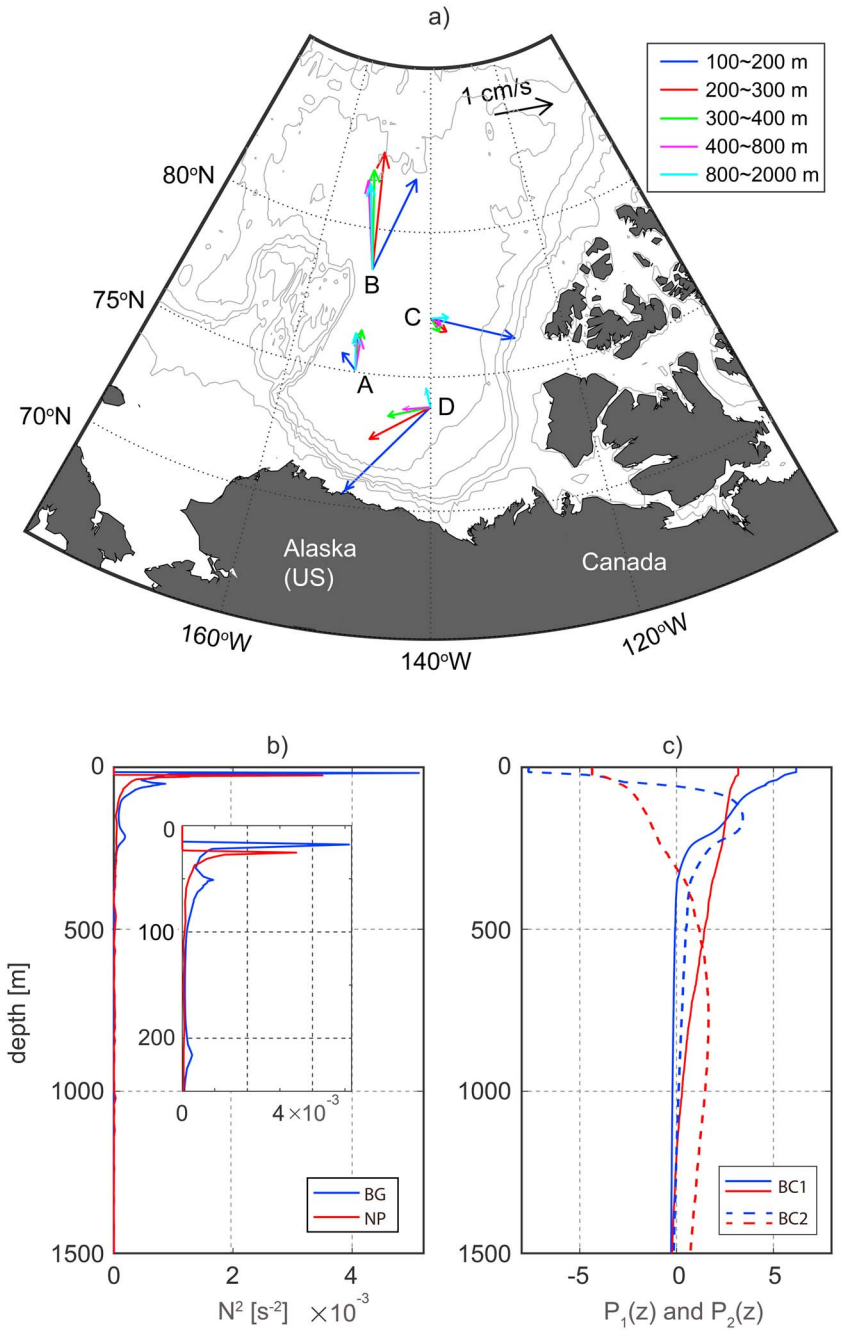

Figure 1. (a) Map of the Canada Basin showing the four mooring locations. The mean flow field is shown at each location. Colored arrows indicate mean velocities in layers of 100–200, 200–300, 300–400, 400–800, and 800–2,000 m. Gray contours are bathymetry of 100, 500, 1,000, 2,000, and 3,000 m. (b) Mean buoyancy frequency profiles from the Beaufort Gyre (BG, blue, from Mooring D) and the North Pacific Ocean (NP, red). (c) Mode structures $P(z)$ for the first two baroclinic modes (solid lines: first baroclinic modes; dashed lines: second baroclinic modes) for Mooring D in the Beaufort Gyre (blue) and the representative North Pacific Ocean (red) stratification profile.

Daily values are available between 1991 and 2015 with a horizontal resolution of 12.5 km. This product has been used effectively and validated in past studies (e.g., Sakov et al., 2017; Xie et al., 2017). Further, a partial time series record of upward-looking acoustic doppler current profiler (ADCP) measurements is available for Moorings A, B (2010–2016), and D (2005–2016); ADCP data are available at http://www.whoi.edu/beaufortgyre. Velocity data from a few meters depth to ~40 m with a vertical resolution of 2 m are returned. We find good agreement between the reanalysis and ADCP velocities, and negligible difference in KE parti-

tioning results whether ADCP velocities or reanalysis surface velocities are employed (i.e., results are insensitive to the exact value of surface velocity). Reanalysis data are not available after 2015, and we use ADCP data for the analyses of data from Moorings A and D for 2015–2016 (Mooring B did not return data in this year).

Finally, we have estimated a mean density profile from hydrographic measurements made near the Kuroshio Current region (in 30°N and 40°N, 150°E and 160°E) between 2003 and 2016 for comparison. Hydrographic data were obtained from the World Ocean Database (https://www.nodc.noaa.gov/OC5/WOD13).

3. Calculation of Vertical Modes

Water column motions in the ocean can be represented as the sum of an infinite number of orthogonal motions with corresponding stratification-dependent vertical modes (i.e., barotropic and baroclinic modes) in the vertical dimension associated with a set of horizontal scales (i.e., Rossby deformation radii; e.g., Gill, 1982). The modes indicate how water column motions of different scales are set by the stratification. Interactions between modes govern how KE is transferred and redistributed in the water column (section 5). To begin, we compute the barotropic and first four baroclinic mode structures for mean Beaufort Gyre stratification measured at the mooring sites and compare and contrast with vertical modes computed for a representative North Pacific stratification.

Following Gill (1982), vertical mode structures can be found by considering the linearized momentum equations with hydrostatic balance, mass, and buoyancy conservation equations. The linearized system may be reduced to two equations in vertical velocity w and pressure p, which may be reduced further by writing variables in separable form as follows: $w(x,y,z,t) = W(z)\tilde{w}(x,y,t)$ and $p(x,y,z,t) = P(z)\tilde{p}(x,y,t)$. The result is the following system (e.g., Gill, 1982, for further details)

$$\frac{\mathrm{d}^2 W(z)}{\mathrm{d}z^2} + \frac{N_0(z)^2}{c^2} W(z) = 0, \tag{1}$$

and

$$\frac{\mathrm{d}}{\mathrm{d}z}\left[\frac{f}{N_0(z)^2}\frac{\mathrm{d}P(z)}{\mathrm{d}z}\right] + \frac{f}{c^2}P(z) = 0, \tag{2}$$

with boundary conditions

$$W(z=0,-H) = 0, \tag{3}$$

$$\left[\frac{\mathrm{d}P(z)}{\mathrm{d}z}\right]\Big|_{z=0,-H} = 0. \tag{4}$$

Here $P(z)$ and $W(z)$ are dimensionless vertical mode structures for horizontal and vertical velocities, respectively (e.g., Gill, 1982; Wunsch & Stammer, 1997). $N_0^2 = -(g/\rho_0)/(\mathrm{d}\bar{\rho}/\mathrm{d}z)$ is the basic-state buoyancy frequency calculated from the mean density field $\bar{\rho}$ over the entire mooring record for a given mooring (Figures 2a and 2b; see Appendix A), ρ_0 is a representative density, f is the Coriolis parameter, and $-H$ is the bottom depth at the mooring in question. We make the assumption here of a flat-bottom ocean and negligible mean background flow. The resting ocean assumption has been discussed at length in past studies (e.g., Szuts et al., 2012; Wunsch, 1997), and it is particularly appropriate here due to the weak background flow (i.e., much weaker than eddy velocities) in the Beaufort Gyre. c is a separation constant associated with the Rossby deformation radius, where $R_d = c/f$ (see Figure 2c); it relates the equations in the horizontal and vertical dimensions (see Wunsch, 2015).

The typical buoyancy frequency of the Beaufort Gyre is characterized by three maxima (Figure 1b, blue), one associated with the mixed layer base and two more within the halocline (associated with Pacific water inflows; Timmermans et al., 2014). Halocline eddies are observed in the water column at depths between these maxima (e.g., Zhao et al., 2014, 2016). The typical stratification of the North Pacific Ocean, on the other hand, is characterized by a single peak in the buoyancy frequency at the thermocline (Figure 1b, red), below which stratification decays with depth. In the upper ocean (shallower than ~300 m), the Beaufort Gyre is more strongly stratified than the North Pacific Ocean (Figure 1b); in the deep ocean (deeper than ~1,000 m), the Beaufort Gyre has a weaker stratification than the North Pacific. The basic-state density (buoyancy frequency) profiles are similar across all Beaufort Gyre moorings (Figures 2a and 2b). We use these mean stratification

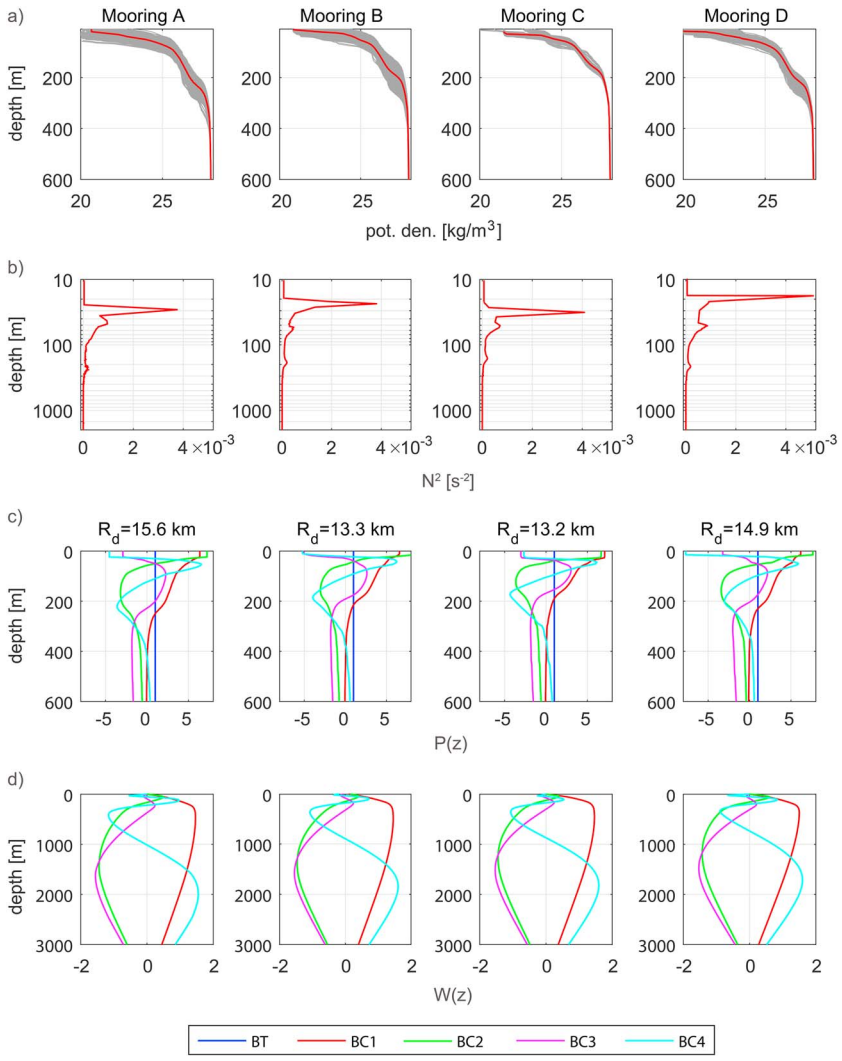

Figure 2. (a) Mean-state potential density (kg/m^3, red solid lines) and potential density from all profiles (gray lines). (b) Mean-state buoyancy frequency (1/s^{-2}, red solid lines). Note that the *y* axis is a log scale. (c) Normalized barotropic and first four baroclinic mode structures $P(z)$ in the upper ocean. $P(z)$ in the deeper ocean does not vary much. The corresponding first baroclinic Rossby deformation radius R_d is shown for each mooring. (d) Normalized first four baroclinic mode structures $W(z)$. The columns are for moorings A, B, C, and D, from left to right.

profiles to compute the structure of each mode at each mooring and for the representative North Pacific profile, solving equations (1)–(4). The calculation of modes requires density profiles from the ocean surface to the bottom; details of the extrapolation and validity are discussed in Appendix A.

For convenient comparison between modes, we normalize such that $\frac{1}{H}\int_{-H}^{0} P_m(z)P_m(z)\mathrm{d}z = 1$ for a given mode m (e.g., Szuts et al., 2012). Note also that vertical modes are orthogonal such that for modes m and n (where $m \neq n$), $\int_{-H}^{0} P_m(z)P_n(z)\mathrm{d}z = 0$. There is negligible difference in mode structures between each of the Beaufort Gyre moorings (Figure 2). Compared to the North Pacific, vertical modes in the Beaufort Gyre are more surface intensified (i.e., they exhibit shallower maxima, Figure 1c). To understand this, let us consider $P_2(z)$, for example (Figure 1c). $P_2(z)$ indicates what the vertical structure of horizontal velocities would be if the water column of a given stratification could be roughly divided into three layers moving in opposite directions between adjacent layers. In the Beaufort Gyre, the more weakly stratified deep water suggests a thicker third (deep) layer and the more strongly stratified upper ocean gives rise to a thinner first (shallow) layer compared to the North Pacific where the upper ocean density increases more gradually. This gives rise to the shallower peak in $P_2(z)$ in the Beaufort Gyre, that is, the more surface-intensified mode structure. It is also helpful to examine the analytical form of the mode structures which can be derived under

the WKB approximation; these do not differ appreciably from the numerical solutions (see Chelton et al., 1998). Conservation of mass suggests that when $W_2(z) = 0$, $P_2(z)$ attains a local maximum. The analytical solution may be written as $W_2(z) = [\frac{N_0(z)}{c_2}]^{-\frac{1}{2}} B \sin[\frac{1}{c_2}\int_{-H}^{z} N_0(z')\mathrm{d}z']$, where B is a constant. The depth of the $P_2(z)$ maximum is then equivalent to finding the depth z_{m_2} satisfying $\int_{-H}^{z_{m_2}} N_0(z')\mathrm{d}z' = \pi c_2$, where $c_2 = \frac{1}{2\pi}\int_{-H}^{0} N_0(z')\mathrm{d}z'$ (see Chelton et al., 1998). We estimate z_{m_2} for the Beaufort Gyre stratification ($z_{m_2} \approx 200$ m) and the North Pacific stratification ($z_{m_2} \approx 730$ m); two factors result in the shallower value in the Beaufort Gyre—the weaker deep stratification and the more strongly stratified halocline.

Now that vertical structures $P(z)$ and $W(z)$ have been computed for each mode (Figure 2), we can estimate the fraction of KE in each of these modes in the Beaufort Gyre.

4. Partitioning Beaufort Gyre KE Into Modes

Water column velocity (u, v, w) can be written as the sum of barotropic and baroclinic vertical modes as follows

$$u(x,y,z,t) = \sum_{m=0}^{\infty} \alpha_{um}(x,y,t)P_m(z), \tag{5}$$

$$v(x,y,z,t) = \sum_{m=0}^{\infty} \alpha_{vm}(x,y,t)P_m(z), \tag{6}$$

$$w(x,y,z,t) = \sum_{m=0}^{\infty} \alpha_{wm}(x,y,t)W_m(z), \tag{7}$$

where α_{um}, α_{vm} and α_{wm} are the mth mode amplitudes for u, v, and w, respectively. $m = 0$ represents the barotropic mode, and $m > 0$ are baroclinic modes. At a given mooring location (x, y), measured velocity (e.g., eastward velocity $u(z, t)$) at time t and depth z can be expressed as the sum of velocity components (i.e., a reconstructed velocity), and we may write

$$\int_{-H}^{0} u(z,t)P_m(z)\mathrm{d}z = \int_{-H}^{0} \alpha_{um}(t)P_m(z)P_m(z)\mathrm{d}z = \alpha_{um}(t). \tag{8}$$

The mode amplitude $\alpha_{um}(t)$ can be calculated if velocity is measured throughout the full depth of the water column (Gill, 1982).

Because the deep Beaufort Gyre is quiescent, velocity deeper than 2,000 m may be extrapolated to be the mean velocity between 1,800 m and the deepest mooring measurement. Variability is much larger in the upper ocean, and extrapolation of velocities shallower than 50 m is not possible. For measurements covering the partial water column or having coarse vertical resolution (e.g., a line of fixed-depth current meters), the Gaussian-Markov inversion method has been used to fit the measured velocity to mode structures (e.g., Szuts et al., 2012; Wunsch, 1997). However, we find this fitting method applied to Beaufort Gyre mooring data returns anomalously large reconstructed velocities at depths shallower than ~50 m due to a lack of constraint on surface velocities. Results are much improved by constraining surface velocities using reanalysis information or upper ocean ADCP data (section 2.2). In this way, we find good fits at depths where mooring velocity data are available, as well as reasonable reconstructed velocities (i.e., surface velocity magnitudes in the range 0–10 cm/s; see, e.g., Armitage et al., 2017) above the shallowest measured depth.

With knowledge of mode amplitudes, and following Wunsch (1997), depth-averaged KE ($\overline{KE}$) over the full water column can be calculated from velocity at a given mooring location (x, y) using Parseval's theorem (see Bracewell, 1986) as

$$\begin{aligned}\overline{KE}(t) &= \frac{1}{H}\int_{-H}^{0}\frac{1}{2}\left[u(z,t)^2 + v(z,t)^2\right]\mathrm{d}z = \frac{1}{2H}\sum_{m=0}^{\infty}[\alpha_{um}(t)^2 + \alpha_{vm}(t)^2]\int_{-H}^{0}P_m(z)^2\mathrm{d}z \\ &= \frac{1}{2H}\sum_{m=0}^{\infty}[\alpha_{um}(t)^2 + \alpha_{vm}(t)^2].\end{aligned} \tag{9}$$

$\overline{KE}$ in the mth mode can be expressed as $\overline{KE}_m = [\alpha_{um}(t)^2 + \alpha_{vm}(t)^2]/(2H)$. The fraction of total KE in the mth mode can be expressed as $\overline{KE}_m/\overline{KE}$.

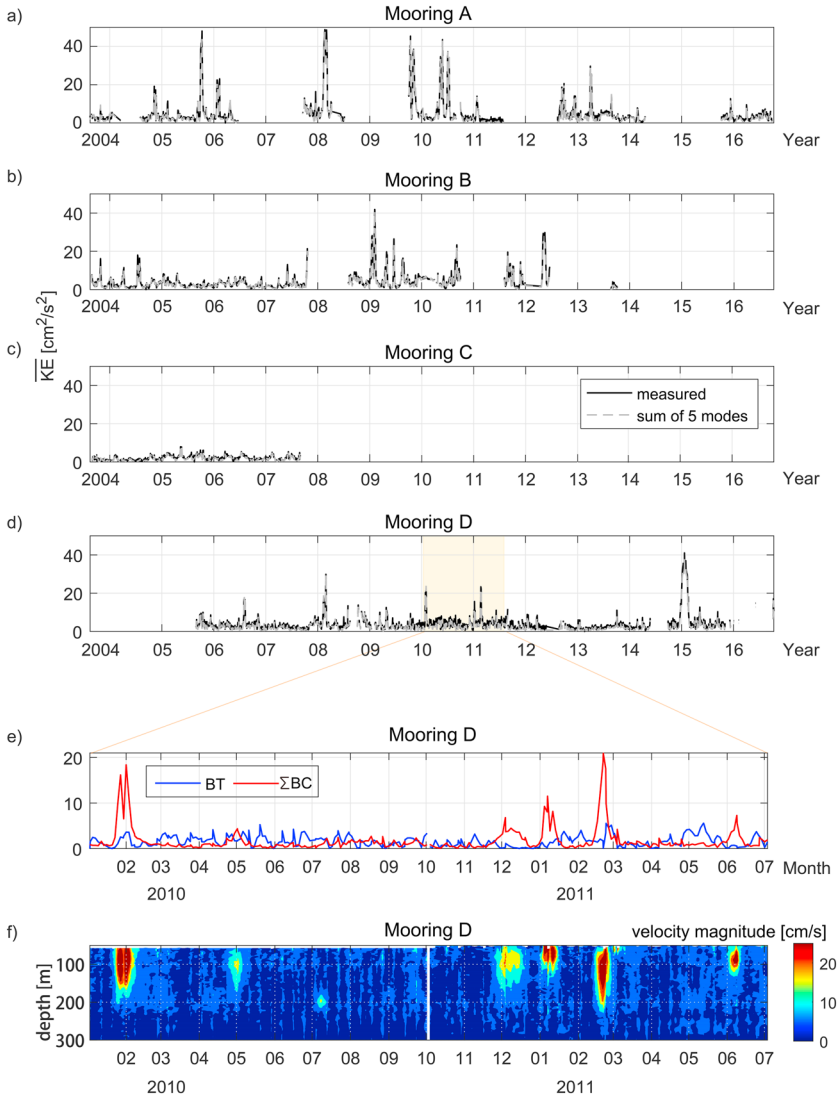

Figure 3. (a–d) Measured column average kinetic energy ($\overline{KE}$ [cm^2/s^2], black lines) and reconstructed $\overline{KE}$ from the first five modes (dashed gray lines) from all four moorings. (e) Column average kinetic energy ($\overline{KE}$ [cm^2/s^2]) inferred from the barotropic mode (blue) and the first four baroclinic modes (red) between January 2010 and July 2011 from Mooring D (the shaded region in panel (d)). (f) Measured profiles of velocity magnitude between 100 and 300 m in the same time period as in (e).

We find that in nearly all cases the sum of the first five modes (barotropic plus first four baroclinic) is sufficient to well represent the measured $\overline{KE}$ (Figure 3). The exception to this is when there are deep eddies present, which have velocity maxima ~1,200m depth (see Carpenter & Timmermans, 2012; Zhao & Timmermans, 2015), and energy is found in higher baroclinic modes. These have negligible influence on halocline dynamics, and for the purposes of this study, deeper eddies have been removed from the record (see Zhao & Timmermans, 2015).

The Beaufort Gyre $\overline{KE}$ is dominated by the halocline eddy field (see Zhao & Timmermans, 2015; Zhao et al., 2016; Figure 3). High $\overline{KE}$ (larger than ~8 cm^2/s^2) is associated with the existence of halocline eddies. Partitioning KE into modes (consider Mooring D, e.g., Figures 3e and 3f) suggests that the sum of the first four baroclinic modes accurately represents halocline mesoscale eddies. In particular, for Moorings A, B, and D, the percentage of total energy found in the first two baroclinic modes is 71%, 63%, and 77% (respectively) when eddies are present. The contributions of each of the two modes are effectively equally important (Figure 4) and independent of the strength of eddies. By contrast, Wunsch (1997) finds the water column KE

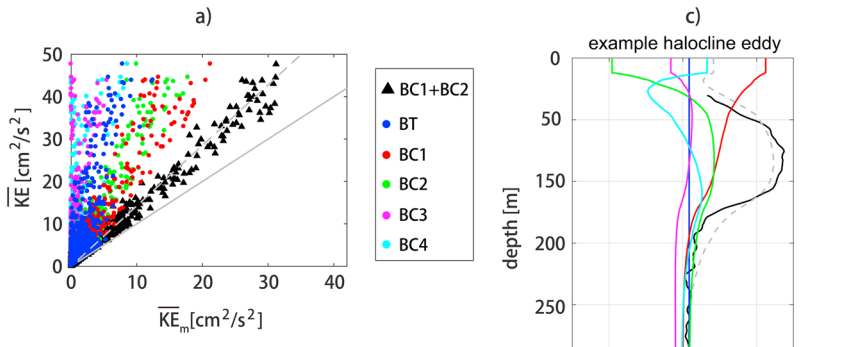

b)

	$\overline{KE_m}$ / $\overline{KE}$		
	A	B	D
BT	18.8%	22.1%	14.4%
BC1	39.5%	39.1%	37.9%
BC2	29.0%	23.1%	36.4%
BC3	4.3%	5.6%	4.9%
BC4	8.4%	10.1%	6.4%

Figure 4. (a) The contribution from each mode (colored dots) and first two baroclinic modes (black triangles, best fit by a dashed line) from Mooring A versus total $\overline{KE}$. The solid gray line has a slope of 1. The dashed gray line shows the best fit result of the sum of the first and second baroclinic modes. (b) The percentage of each mode in explaining $\overline{KE}$ (when an eddy passes the mooring). Note that Mooring C, which recorded negligible eddy activity, is not included. (c) Profiles of measured eastward velocity (black solid lines), reconstructed eastward velocity from the sum of the first five modes (gray dashed lines) and eastward velocity from each of the first five modes (colored lines) for a typical halocline eddy.

for the midlatitude oceans to be predominately in the barotropic and first baroclinic mode (around 40% and 50% of KE, respectively, with spatial variations). In general, deeper eddies may result in a higher percentage of KE in higher modes (e.g., Clement et al., 2014). It is important to note that the eddies sampled here are located between ~100 and ~250m depth, due to the limited depth range sampled by the moorings. The ability to sample shallower eddies may yield more energy in the first baroclinic mode, which may decrease the percentage of KE in the second baroclinic mode. However, the Beaufort Gyre will still be characterized by a significant percentage of KE in the second baroclinic mode because of the large numbers of halocline eddies.

To understand the distribution of KE within modes in the Beaufort Gyre, and in particular why KE partitioning in the mid-latitude oceans differs, in the next section we consider conservation of quasi-geostrophic potential vorticity for a specified stratification to understand how energy may be redistributed between modes, and to quantify the efficiency of this redistribution.

5. KE Pathways in the Beaufort Gyre

Geostrophic turbulence theory predicts that there is an inverse energy cascade from higher baroclinic modes to the barotropic mode via mode-mode interactions related to the advection of barotropic and baroclinic KE (e.g., Charney, 1971; Fu & Flierl, 1980; Hua & Haidvogel, 1986; Salmon, 1980). However, the efficiency of this KE transfer in the vertical greatly depends on the stratification (Smith & Vallis, 2001). The observation of KE in the midlatitude oceans being found almost entirely in the barotropic and first baroclinic modes (Wunsch, 1997) is explained by inefficient energy transfer to the barotropic mode (for typical thermocline stratification), and as a result a significant portion of energy remains in the first baroclinic mode. The difference in the dominant energy-containing modes between the Beaufort Gyre and the midlatitude oceans suggests different energy flow pathways. We test this hypothesis by comparing interactions between different vertical modes for differing stratifications.

Smith and Vallis (2001) examine the energy distribution in the vertical for nonuniform thermocline stratification (which they express as an analytical function of depth). They calculate vertical normal modes given

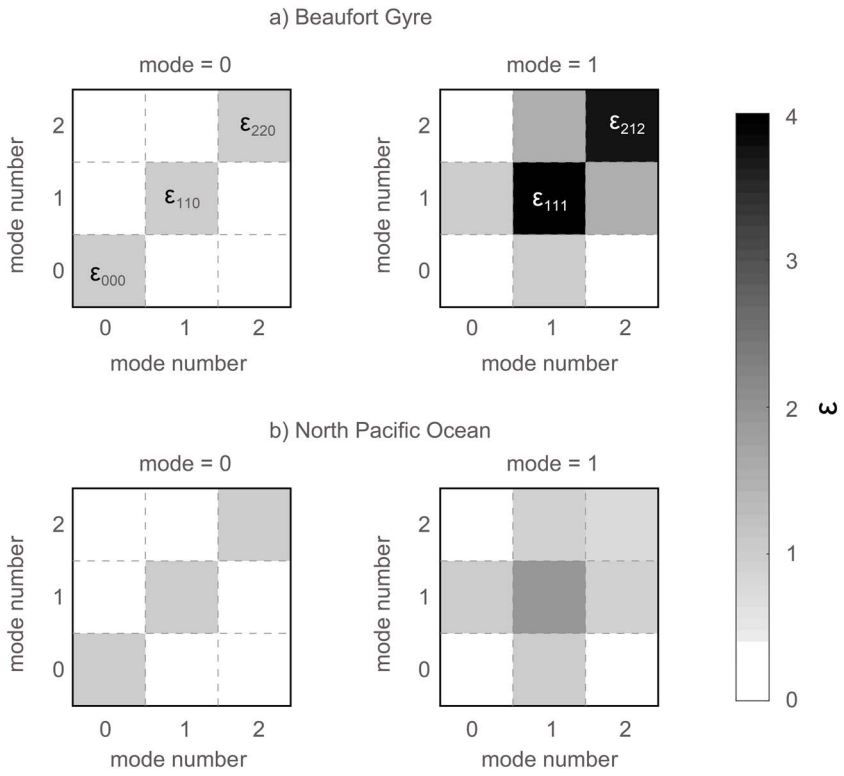

Figure 5. The interaction coefficient ϵ calculated from the representative buoyancy frequency profiles (Figure 1) from (a) the Beaufort Gyre and (b) the North Pacific Ocean. The x axis, y axis, and title each represent a mode such that each square in a panel represents the magnitude of an interaction coefficient (see, e.g., the labeled squares in the top panels).

this stratification, and then considering a quasi-geostrophic system, estimate how the potential vorticity in one mode may be altered by flow interactions in other modes. The efficiency of this process as a function of mode is estimated by *interaction coefficients*. Here we apply the same formalism as Smith and Vallis (2001) to the Beaufort Gyre stratification and evaluate KE pathways there.

Mode-mode interactions can be quantified by considering quasi-geostrophic potential vorticity (PV) conservation on an f-plane (with no external forcing)

$$\frac{\partial q}{\partial t} = -\frac{\partial \psi}{\partial x}\frac{\partial q}{\partial y} + \frac{\partial \psi}{\partial y}\frac{\partial q}{\partial x}, \tag{10}$$

where $q(x,y,z,t) = (\nabla^2 + \frac{\partial}{\partial z}\frac{f^2}{N_0(z)^2}\frac{\partial}{\partial z})\psi(x,y,z,t)$, $\nabla^2 = \partial^2/\partial x^2 + \partial^2/\partial y^2$, and ψ is a stream function where $u = -\partial\psi/\partial y$ and $v = \partial\psi/\partial x$.

Just as for the velocity (section 3), ψ and q may also be represented as the sum of modes as $\psi(x,y,z,t) = \sum_{m=0}^{\infty}\psi_m(x,y,t)P_m(z)$ and $q(x,y,z,t) = \sum_{m=0}^{\infty}q_m(x,y,t)P_m(z)$. This decomposition in (10) yields the change of PV in the mth mode (Flierl, 1978)

$$\frac{\partial q_m}{\partial t} = \sum_{i,j}\left[\frac{\partial \psi_i}{\partial y}\frac{\partial q_j}{\partial x} - \frac{\partial \psi_i}{\partial x}\frac{\partial q_j}{\partial y}\right]\epsilon_{ijm}, \tag{11}$$

where $i,j,m = 0,1,2,\ldots$ represent mode numbers, ψ_i and q_i are the ith mode amplitudes for ψ and q, and $\epsilon_{ijm} = \frac{1}{H}\int_{-H}^{0}P_i(z)P_j(z)P_m(z)\mathrm{d}z$ is an interaction coefficient between modes i, j and m.

Equation (11) can be understood as the advection from velocity in the ith mode of the PV in the jth mode producing a change in the mth mode PV (see, e.g., Flierl, 1978). The interaction coefficient ϵ_{ijm} characterizes how much energy is transferred between modes i, j, and m and depends upon the stratification. We showed how the more surface-intensified structure of modes in the Beaufort Gyre compared to the North Pacific relates to the Beaufort Gyre's more strongly stratified upper water column and weakly stratified deep water column. This gives rise to larger magnitude interaction coefficients between baroclinic modes because

the modes with higher variation and largest amplitude are concentrated in the upper ocean (Figure 5a). Smith and Vallis (2001), for example, find that a thinner thermocline thickness can reduce the efficiency of energy transferred to the barotropic mode, leading to a concentration of energy in the first baroclinic mode.

For the North Pacific Ocean stratification, we find ε to be consistent with Smith and Vallis (2001) with a higher value of ε_{111} compared to ε_{110}, suggesting that interactions in the first baroclinic mode promote energy to remain there rather than transfer to the barotropic mode (Figure 5b). As a result, most KE in the North Pacific is found in both the barotropic and the first baroclinic modes. In the Beaufort Gyre, ε_{111} and ε_{212} are higher than ε_{110}, indicating that energy transfer between baroclinic modes in the Beaufort Gyre is more efficient than to the barotropic mode (Figure 5a). In sum, halocline eddies in the Beaufort Gyre have a greater barrier to vertical homogeneity (Charney, 1971), consistent with a lower percentage (compared to the North Pacific Ocean) of eddy KE in the Beaufort Gyre being in the barotropic mode. Further note that ε_{212} is of similar magnitude as ε_{111} in the Beaufort Gyre. Large ε_{212} suggests that the interaction between the first and second baroclinic modes will result in PV production in the second baroclinic mode. This explains the dominance of the second baroclinic mode energy in the Beaufort Gyre.

It is important to note that the energy transfer across vertical modes requires the presence of an active turbulent field (i.e., interacting eddies that advect each other's potential vorticity). However, observations suggest that halocline eddies are coherent isolated features rather than components of an active turbulent field. Thus, an explanation of KE mode partitioning requires distinguishing between the following two limiting cases: (1) eddies form with a particular energy partitioning because of the baroclinic structure of unstable currents that produced them (i.e., the fastest growing mode has a certain vertical energy partitioning) and (2) eddies form due to a wide range of unstable flows but the observed eddies favor a specific mode energy distribution due to strong vertical mode interactions (that depend only on the vertical stratification). Resolving this distinction will require more comprehensive observations of the eddy field than are available at present, as well as numerical modeling.

6. Summary and Discussion

Water column KE in the Beaufort Gyre is dominated by halocline eddies and can be represented as a sum of the barotropic and first two baroclinic modes. More than 85% of the water column KE is accounted for in the barotropic and first two baroclinic modes. We show that this KE partitioning is the result of mode-mode interactions (determined by the halocline stratification). The efficiency of energy transfer to the barotropic mode is relatively low. There is a stronger tendency, for example, for interaction between the first and second baroclinic modes to concentrate energy in the second baroclinic mode. The KE partitioning differs from the midlatitude oceans (e.g., Wunsch, 1997) where energy is primarily concentrated in the barotropic and the first baroclinic modes because the stratification is weaker and less surface intensified than in the Beaufort Gyre.

In their mode-mode analysis, Smith and Vallis (2001) used the nondimensional analytical expression $N_0^2(z) = e^{z/\delta}/\delta$ for stratification where depth $z = [-1, 0]$. This stratification is varied from more surface intensified to uniform, corresponding to typical stratification profiles in the midlatitude ocean ($\delta = 0.05$) and the troposphere ($\delta \sim \infty$). The typical stratification in the Beaufort Gyre is too complex to be represented by this expression, although the general pattern of weakly stratified deep and strongly stratified upper ocean is characterized by $\delta < 0.05$. The corresponding interaction coefficient based on this stratification is consistent with our estimates here: a more strongly stratified upper ocean (i.e., smaller δ) gives rise to a larger efficiency of KE transfer between baroclinic modes than to the barotropic mode, as well as an energy concentration in higher baroclinic modes.

Our study is limited here to an assessment of how KE is redistributed vertically in the water column at a given location. We do not have sufficient spatial coverage in data to analyze KE in the horizontal plane. That is, we cannot quantify the evolution of PV as expressed in parentheses on the right-hand side of equation (11). Theory suggests that the relevant horizontal scale of the mth mode is the mth Rossby deformation radius (e.g., Hua & Haidvogel, 1986; Smith & Vallis, 2001). Beaufort Gyre halocline eddies have a significant portion of their energy in the second baroclinic mode, and eddies generally have length scales in the range R_{d_1} and R_{d_2}. The location of moorings further restricts our study of KE evolution to the abyssal plain.

Our analysis points to the importance of stratification in the evolution of KE in the Beaufort Gyre, and this is helpful in understanding how energy is dissipated. Friction is the ultimate sink of KE, either operating on

motions at the smallest scales (e.g., Dewar & Hogg, 2010; Nikurashin et al., 2013; Zhai et al., 2010) or associated with drag at topographic boundaries (e.g., Nikurashin et al., 2013), including sea ice cover (e.g., Ou & Gordon, 1986). The transfer of KE to the first baroclinic and barotropic modes provides a mechanism for topographic interactions. The inefficiency of energy transfer to the barotropic mode may imply less efficient KE dissipation in the Beaufort Gyre through bottom drag. The upper boundary, where the surface ocean is in contact with sea ice for most of the year, may play an important role in KE dissipation in the Beaufort Gyre when KE is transferred to the first baroclinic mode. Future work will focus on understanding the dissipation of KE in the Beaufort Gyre, in particular how the interaction between mesoscale motions and the underside of sea ice contributes to dissipating KE.

It is important to point out that in this paper we used the traditional orthogonal basis (i.e., barotropic and baroclinic modes), which requires the assumption of a rigid lid and vanishing vertical velocity at this top boundary. Further, it assumes no bottom slope nor bottom friction. Other studies have introduced different formalisms motivated by the aim to infer the vertical structure of ocean flows from satellite observations of the surface ocean. In one formalism, ocean flows are considered to be driven by surface buoyancy gradients and a surface quasi-geostrophic stream function is introduced (see, e.g., Lapeyre, 2009; Smith & Vanneste, 2013). The vertical velocity structure then depends upon the surface horizontal structure. A further development accounts for a bottom slope and/or bottom friction (see, e.g., de La Lama et al., 2016; LaCasce, 2017); solutions indicate that bottom velocities tend to 0 when bottom slope and/or friction are taken into account, which gives rise to surface-intensified modes. A future study could employ the above methods in the Canada Basin, and results could be compared to those found here using the traditional orthogonal basis.

Idealized numerical experiments and theory have been put forward to describe a mechanism for wind-driven gyre equilibration by eddies that cumulatively act to flatten isopycnals and inhibit freshwater accumulation (Manucharyan et al., 2016, 2017). However, likely due to the simplicity of the vertical stratification used in these idealized experiments, the generated eddies were not coherent and predominantly of the first baroclinic mode with substantially larger sizes O(100 km) compared to the observed isolated halocline eddies which have significant second baroclinic mode energy and are O(10 km) in size. Nevertheless, mooring estimates of O(100 km) mixing length scales and eddy diffusivities O(50–400 m^2/s) are in agreement with numerical experiments of Manucharyan and Spall (2015), suggesting that the along-isopycnal stirring occurs on substantially larger scales than the scale of isolated halocline eddies (Meneghello et al., 2017). Reconciling differences between the modeled and observed eddy characteristics and understanding eddy-mean flow interactions by relating the eddy KE mode partitioning to the cumulative eddy transport of tracers such as freshwater remain an open challenge.

Appendix A: Calculating the Vertical Structure of Modes: Extrapolating Mooring Measurements in Depth

Mode structures $W(z)$ and $P(z)$ require a representative buoyancy frequency profile over the entire water column depth (i.e., 0 to ~3,800 m), while mooring MMPs only sample part of the water column (i.e., ~60 to ~2,000 m). We extend the MMP density profiles above the shallowest and below the deepest measurements using CTD data sampled at the same location during the BGEP/Joint Ocean Ice Studies expedition of the same year as the MMP profiles.

To examine the sensitivity of the resulting modes to seasonal variation in surface stratification, we use year-round ITP (~7 to ~750 m) estimates for the seasonally varying stratification. Density in the deep Arctic remains nearly the same over time scales of at least a few decades (see Zhao et al., 2014). As an example case, we choose ITP summer measurements from 28 August 2011 at 77.05 textdegreeN, 139.32°W and ITP winter measurements from 6 February 2007 at 77.06°N, 140.69°W, which coincide approximately with the location of Mooring C. Comparing the first four baroclinic mode structures using mooring data extrapolated with the ITP summer profile and that extrapolated with the ITP winter profile (Figure A1), we find that there is effectively no difference and seasonal variations in the upper water column can be neglected. Examination across all moorings yields the same result.

Therefore, the mean-state stratification N_0, required in the calculation of mode structures, is estimated from each CTD-extrapolated MMP profile. This is done using potential density profiles by estimating the mean depth of each isopycnal over the entire mooring measurement record of about 12 years for Moorings A,

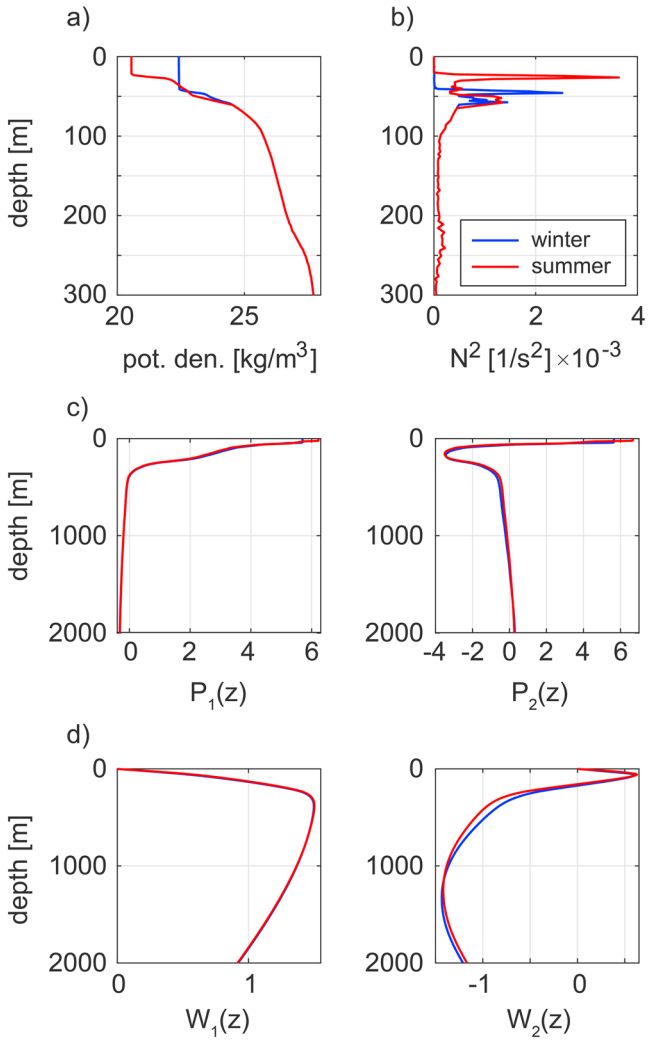

Figure A1. Influence of upper ocean extrapolation using measurements from winter (blue, from ITP 6 on 6 February 2007) and summer (red, from ITP 54 on 28 August 2011). These two profiles are chosen to be the closest to the Mooring C location. (a, b) Mean potential density and buoyancy frequency of Mooring C extrapolated using ITP profiles above 60 m. Deep values are extrapolated using the CTD data, as described in section 3. (c, d) The first two baroclinic mode structures $W(z)$ and $P(z)$.

B, and D and about 4 years for Mooring C (Figure 2a). The mean buoyancy frequency is then calculated from this mean potential density profile (Figure 2b). Note that the presence of eddies does not influence the mean buoyancy frequency profile. A density profile through an eddy differs from a profile where there is no eddy in that there is a nearly uniform density through an eddy core. However, the thickness of this difference (i.e., the thickness of an eddy core) ranges from ~20 to ~200 m, only 0.5% to 5% of the entire water column. Further, only a small fraction (~10%) of MMP profiles sample eddies.

Acknowledgments
Mooring data were collected and made available by the Beaufort Gyre Exploration Program based at the Woods Hole Oceanographic Institution (http://www.whoi.edu/beaufortgyre) in collaboration with researchers from Fisheries and Oceans Canada at the Institute of Ocean Sciences. Funding was provided by the National Science Foundation Division of Polar Programs under award 1107623. We appreciate the support and helpful scientific discussions associated with the Forum for Arctic Modeling and Observational Synthesis (FAMOS) and the FAMOS School for Young Arctic Scientists. We thank Andrey Proshutinsky and John Marshall for helpful comments.

References

Armitage, T. W., Bacon, S., Ridout, A. L., Petty, A. A., Wolbach, S., & Tsamados, M. (2017). Arctic Ocean geostrophic circulation, 2003–2014. *The Cryosphere Discuss*, *11*, 1767–1780. https://doi.org/10.5194/tc-2017-22

Bracewell, R. N. (1986). *The Fourier Transform and its Applications* (Vol. 31999). New York: McGraw-Hill.

Carpenter, J. R., & Timmermans, M.-L. (2012). Deep mesoscale eddies in the Canada Basin, Arctic Ocean. *Geophysical Research Letters*, *39*, L20602. https://doi.org/10.1029/2012GL053025

Charney, J. G. (1971). Geostrophic turbulence. *Journal of the Atmospheric Sciences*, *28*(6), 1087–1095. https://doi.org/10.1175/1520-0469(1971)028<1087:GT>2.0.CO;2

Chelton, D. B., Deszoeke, R. A., Schlax, M. G., El Naggar, K., & Siwertz, N. (1998). Geographical variability of the first baroclinic Rossby radius of deformation. *Journal of Physical Oceanography*, *28*(3), 433–460. https://doi.org/10.1175/1520-0485(1998)028<0433:GVOTFB>2.0.CO;210.1029/2010GL046063

Clement, L., Frajka-Williams, E., Szuts, Z. B., & Cunningham, S. A. (2014). Vertical structure of eddies and Rossby waves, and their effect on the Atlantic meridional overturning circulation at 26.5 n. *Journal of Geophysical Research: Oceans*, *119*, 6479–6498. https://doi.org/10.1002/2014JC010146

de La Lama, M. S., LaCasce, J. H., & Fuhr, H. K. (2016). The vertical structure of ocean eddies. *Dynamics and Statistics of the Climate System*, *1*(1). https://doi.org/10.1093/climsys/dzw001

Dewar, W. K., & Hogg, A. M. (2010). Topographic inviscid dissipation of balanced flow. *Ocean Modelling*, *32*(1), 1–13. https://doi.org/10.1016/j.ocemod.2009.03.007

Flierl, G. R. (1978). Models of vertical structure and the calibration of two-layer models. *Dynamics of Atmospheres and Oceans*, *2*(4), 341–381. https://doi.org/10.1016/0377-0265(78)90002-7

Fu, L., & Flierl, G. R. (1980). Nonlinear energy and enstrophy transfers in a realistically stratified ocean. *Dynamics of Atmospheres and Oceans*, *4*(4), 219–261. https://doi.org/10.1016/0377-0265(80)90029-9

Gill, A. E. (1982). *Atmosphere–Ocean Dynamics* (pp. 162). New York: Academic Press.

Holland, W. R. (1978). The role of mesoscale eddies in the general circulation of the ocean – Numerical experiments using a wind-driven quasi-geostrophic model. *Journal of Physical Oceanography*, *8*(3), 363–392. https://doi.org/10.1175/1520-0485(1978)008<0363:TROMEI>2.0.CO;2

Hua, B. L., & Haidvogel, D. B. (1986). Numerical simulations of the vertical structure of quasi-geostrophic turbulence. *Journal of the Atmospheric Sciences*, *43*(23), 2923–2936. https://doi.org/10.1175/1520-0469(1986)043<2923:NSOTVS>2.0.CO;2

Krishfield, R. A., Proshutinsky, A., Tateyama, K., Williams, W. J., Carmack, E. C., McLaughlin, F. A., & Timmermans, M. L. (2014). Deterioration of perennial sea ice in the Beaufort Gyre from 2003 to 2012 and its impact on the oceanic freshwater cycle. *Journal of Geophysical Research*, *119*, 1271–1305. https://doi.org/10.1002/2013JC008999

Krishfield, R., Toole, J., Proshutinsky, A., & Timmermans, M.-L. (2008). Automated Ice-Tethered Profilers for seawater observations under pack ice in all seasons. *Journal of Atmospheric and Oceanic Technology*, *25*(11), 1092–2105. https://doi.org/10.1175/2008JTECHO587.1

LaCasce, J. H. (2017). The prevalence of oceanic surface modes. *Geophysical Research Letters*, *44*, 11,097–11,105. https://doi.org/10.1002/2017GL075430

Lapeyre, G. (2009). What vertical mode does the altimeter reflect? On the decomposition in baroclinic modes and on a surface-trapped mode. *Journal of Physical Oceanography*, *39*(11), 2857–2874.

Manley, T. O., & Hunkins, K. (1985). Mesoscale eddies of the Arctic Ocean. *Journal of Geophysical Research*, *90*(C3), 4911–4930. https://doi.org/10.1029/JC090iC03p04911

Manucharyan, G. E., & Spall, M. A. (2015). Wind driven freshwater buildup and release in the Beaufort Gyre constrained by mesoscale eddies. *Geophysical Research Letters*, *43*, 273–282. https://doi.org/10.1002/2015GL065957

Manucharyan, G. E., Spall, M. A., & Thompson, A. F. (2016). A theory of the wind-driven Beaufort Gyre variability. *Journal of Physical Oceanography*, *46*(11), 3263–3278. https://doi.org/10.1175/JPO-D-16-0091.1

Manucharyan, G., Thompson, A. F., & Spall, M. A. (2017). Eddy memory mode of multidecadal variability in residual-mean ocean circulations with application to the Beaufort Gyre. *Journal of Physical Oceanography*, *47*(4), 855–866. https://doi.org/10.1175/JPO-D-16-0194.1

Manucharyan, G. E., & Timmermans, M.-L. (2013). Generation and separation of mesoscale eddies from surface ocean fronts. *Journal of Physical Oceanography*, *43*(12), 2545–2562. https://doi.org/10.1175/JPO-D-13-094.1

Meneghello, G., Marshall, J., Cole, S. T., Timmermans, M.-L., & Scott, J. (2017). Observational inferences of lateral eddy diffusivity in the halocline of the Beaufort Gyre. *Geophysical Research Letters*, *44*, 12,331–12,338. https://doi.org/10.1002/2017GL075126

Nikurashin, M., Vallis, G. K., & Adcroft, A. (2013). Routes to energy dissipation for geostrophic flows in the Southern Ocean. *Nature Geoscience*, *6*(1), 48–51. https://doi.org/10.1038/ngeo1657

Ou, H.-W., & Gordon, A. L. (1986). Spin-down of baroclinic eddies under sea ice. *Journal of Geophysical Research*, *91*, 7623–7630.

Pedlosky, J. (1979). *Geophysical Fluid Dynamic* (p. 624). New York: Springer.

Pickart, R. S., Weingartner, T. J., Pratt, L. J., Zimmermann, S., & Torres, D. J. (2005). Flow of winter-transformed Pacific water into the Western Arctic. *Deep Sea Research*, *52*(24), 3175–3198. https://doi.org/10.1016/j.dsr2.2005.10.009

Proshutinsky, A., Dukhovskoy, D., Timmermans, M.-L., Krishfield, R., & Bamber, J. L. (2015). Arctic circulation regimes. *Philosophical Transactions of the Royal Society*, *373*(2052), 20140160. https://doi.org/10.1098/rsta.2014.0160

Proshutinsky, A., Krishfield, R., Timmermans, M.-L., Toole, J., Carmack, E., McLaughlin, F., et al. (2009). Beaufort Gyre freshwater reservoir: State and variability from observations. *Journal of Geophysical Research*, *114*, 1271–1305. https://doi.org/10.1002/2013JC008999

Sakov, P., Counillon, F., Bertino, L., Lisater, K. A., Oke, P. R., & Korablev, A. (2017). TOPAZ4: an ocean-sea ice data assimilation system for the North Atlantic and Arctic. *Ocean Science*, *8*(4), 633–656. https://doi.org/10.5194/os-8-633-2012

Salmon, R. (1980). Baroclinic instability and geostrophic turbulence. *Geophysical and Astrophysical Fluid Dynamics*, *15*(1), 167–211. https://doi.org/10.1080/03091928008241178

Smith, K. S., & Vallis, G. K. (2001). The scales and equilibration of midocean eddies: Freely evolving flow. *Journal of Physical Oceanography*, *31*, 554–571. https://doi.org/10.1175/1520-0485(2001)031<0554:TSAEOM>2.0.CO;2

Smith, K. S., & Vanneste, J. (2013). A surface-aware projection basis for quasigeostrophic flow. *Journal of Physical Oceanography*, *43*(3), 548–562.

Szuts, Z. B., Blundell, J. R., Chidichimo, M. P., & Marotzke, J. (2012). A vertical-mode decomposition to investigate low-frequency internal motion across the Atlantic at 26° n. *Ocean Science*, *8*(3), 345–367.

Timmermans, M. L., Proshutinsky, A., Golubeva, E., Jackson, J. M., Krishfield, R., McCall, M., et al. (2014). Mechanisms of Pacific summer water variability in the Arctic's Central Canada Basin. *Journal of Geophysical Research: Oceans*, *119*, 7523–7548. https://doi.org/10.1002/2014JC010273

Timmermans, M. L., Toole, J., Proshutinsky, A., Krishfield, R., & Plueddemann, A. (2008). Eddies in the Canada Basin, Arctic Ocean, observed from ice-tethered profilers. *Journal of Physical Oceanography*, *38*(1), 133–145. https://doi.org/10.1175/2007JPO3782.1

Toole, J. M., Krishfield, R. A., Timmermans, M.-L., & Proshutinsky, A. (2011). The ice-tethered profiler: Argo of the arctic. *Oceanography*, *24*(3), 126–135. https://doi.org/10.5670/oceanog.2011.64

Vallis, G. K. (2006). *Atmosphere and Ocean Fluid Dynamics* (p. 745). Cambridge, UK: Cambridge University Press.

Wunsch, C. (1997). The vertical partition of oceanic horizontal kinetic energy. *Journal of Physical Oceanography*, *27*, 1770–1794. https://doi.org/10.1175/1520-0485(1997)027<1770:TVPOOH>2.0.CO;2

Wunsch, C. (2015). *Modern Observational Physical Oceanography: Understanding the Global Ocean* (p. 141). Princeton: Princeton University Press.

Wunsch, C., & Stammer, D. (1997). Atmospheric loading and the oceanic inverted barometer effect. *Reviews of Geophysics*, *35*, 79–107. https://doi.org/10.1029/96RG03037

Xie, J., Bertino, L., Counillon, F., Lisater, K. A., & Sakov, P. (2017). Quality assessment of the TOPAZ4 reanalysis in the Arctic over the period 1991-2013. *Ocean Science*, *13*(1), 123–144. https://doi.org/10.5194/os-13-123-2017

Zhai, X., Johnson, H. L., & Marshall, D. P. (2010). Significant sink of ocean-eddy energy near western boundaries. *Nature Geoscience*, *3*(9), 608–612. https://doi.org/10.1038/ngeo943

Zhang, J., Steele, M., Runciman, K., Dewey, S., Morison, J., Lee, C., et al. (2016). The Beaufort Gyre intensification and stabilization: A model-observation synthesis. *Journal of Geophysical Research: Oceans*, *121*, 7933–7952. https://doi.org/10.1002/2016JC012196

Zhao, M., & Timmermans, M.-L. (2015). Vertical scales and dynamics of eddies in the Arctic Ocean's Canada Basin. *Journal of Geophysical Research: Oceans*, *120*, 8195–8209. https://doi.org/10.1002/2015JC011251

Zhao, M., Timmermans, M.-L., Cole, S., Krishfield, R., Proshutinsky, A., & Toole, J. (2014). Characterizing the eddy field in the Arctic Ocean halocline. *Journal of Geophysical Research: Oceans*, *119*, 8800–8817. https://doi.org/10.1002/2014JC010488

Zhao, M., Timmermans, M.-L., Cole, S., Krishfield, R., & Toole, J. (2016). Evolution of the eddy field in the Arctic Ocean's Canada Basin, 2005–2015. *Geophysical Research Letters*, *43*, 8106–8114. https://doi.org/10.1002/2016GL069671